

# Introducing Mag-Nets: Rapidly Bending Electromagnetic Actuators for Self-contained Soft Robots

Georgios Bolanakis and Evangelos Papadopoulos, *Life Fellow, IEEE*

**Abstract**—Present electromagnetic soft actuators rely on external magnetic fields or power supplies, while the very few that operate autonomously produce weak actuating forces, limiting their practicality. This work introduces a novel current-controlled electromagnetic actuator that employs copper coils and permanent magnets to produce substantial driving forces. The actuator can serve as a building block for independently controlled actuating networks to develop sophisticated self-contained soft robots and grippers. The design, inspired by fast pneu-net (fPN) actuators, ensures minimal bending resistance from the silicone body and, thus, allows high-speed bending motions. Two applications of the prototype actuator are studied; a two-fingered soft gripper realizing bending speeds of up to 1491 °/s and maximum grasping force of 1.19 N, and an entirely self-contained crawling soft robot utilizing friction anisotropy to generate forward locomotion. A lumped-element model is developed and validated experimentally to describe the dynamics of the gripper's soft finger. Pick-and-place tasks on various targets, and tests on the crawling robot demonstrate, overall, the effectiveness of the developed actuator. The uniqueness of Mag-Nets, lying in their control simplicity, enhanced capability and cost-effectiveness, sets the foundations for a new design approach for soft robots and grippers.

**Index Terms**—Soft sensors and actuators, soft robot materials and design, modeling soft robots, soft robot applications.

## I. INTRODUCTION

SOFT robots pave the way for more compliant and harmless interaction with humans. Contrary to rigid robots that suffer from maneuverability issues and safety limitations overrides, the intrinsic compliance of soft robots allows effortless adaptation to complex and congested environments. Several actuation technologies have been developed to control soft robots, each one demonstrating specific advantages and constraints [1]-[2]. Common actuation types are pneumatic [3]-[4], hydraulic [5]-[6], cable-driven [7]-[8], shape memory alloy based [9]-[10] and magnetic/ electromagnetic [11]-[12]. The latter can be further subcategorized depending on the necessity of external static or dynamically controlled magnetic fields to *environment dependent* and *environment independent* [13].

Manuscript received: January 14 2024; Revised: March 20 2024; Accepted April 3 2024. This paper was recommended for publication by Editor Yong-Lae Park upon evaluation of the Associate Editor and Reviewers' comments. This research work was supported by the project "Applied Research for Autonomous Robotic Systems" (MIS5200632) which is implemented within the framework of the National Recovery and Resilience Plan (NNRP) "Greece 2.0" (Measure: 16618- Basic and Applied Research) and is funded by the European Union-NextGenerationEU.

The authors are with the Athena RC Robotics Institute, Marousi, 15125, Greece, and with the School of Mechanical Engineering, National Technical University of Athens (e-mail: {g.bolanakis, egpapado}@athenarc.gr).

Digital Object Identifier (DOI): see top of this page.

Yet, a common advantage of these actuators is their rapid response, enabling fast and accurate controlled motions.

The use of environment dependent magnetic actuators has attracted considerable interest by the soft robotics community. MagWorm, a worm-like magnet-embedded soft robot, developed by Hanqing et al., can generate biomimetic crawling locomotion using an external moving magnet system [14]. Entirely soft magnetically responsive actuators based on castable silicone resins, loaded with magnetic particles, and under the action of an external magnetic field were proposed for use in pick-and-place and lifting tasks by Carpenter et al. in [15]. Recently, Guoyong Mao et al. developed small-scale soft electromagnetic robots with liquid metal (LM) coils and external permanent magnets that generate a variety of locomotion modes including jumping and swimming [16].

Few cases of environment independent electromagnetic actuators can be found in the literature. Kohls et al. developed an entirely soft electromagnetic actuator that mimics Xenia coral pulsing and grasping motions using LM coils and compliant magnets [17]. LM coils can also be combined with permanent magnets to produce stronger controlled motion of soft robots [13][18]. Despite the use of permanent magnets, the produced actuating forces remain weak due to the use of LM coils. Notably, both designs rely on external power supply and current driving systems to function. In a rare example of rigid coils and magnets combination, Wang et al. developed an externally powered small-scale soft robot inspired by kangaroo hopping motion [19]. The robot is composed by a magnet and a coil in a silicone body. Another work introduces a self-contained, self-powered worm-like soft robot with rigid coils and magnets [20]; however, additional rigid components are used to couple individual actuators together and, by design, high resistance is produced from the silicone body, dropping its efficiency and limiting its application prospects.



Fig. 1. A prototype soft gripper based on the developed electromagnetic actuator firmly grasps and lifts an onion.

In this work, a novel electromagnetic actuator is presented for developing untethered, entirely self-contained and compact soft robots and grippers (Fig. 1). The actuator incorporates copper coils and neodymium permanent magnets embedded in a silicone body inspired by fPN actuators [4], increasing the exerted forces and extending the actuator's application field against existing state-of-the-art electromagnetic-type actuators.

By design, during actuation the bending resistance from the silicone body is minimal allowing high-speed bending motions and large actuating forces. Despite the use of rigid components, the actuator maintains the intrinsic compliance and flexibility of the entirely soft actuators. Two case studies employing the actuator are investigated: a two-fingered soft gripper and a self-contained, self-powered crawling soft robot. A simple yet robust lumped-element model is introduced and validated experimentally to describe the dynamics of the soft finger. The gripper completes multiple pick-and-place tasks, while the crawling robot generates forward locomotion of 8.3 mm/s, demonstrating the overall effectiveness of the actuator. The paper concludes with a thorough discussion of the advantages and limitations of this design, along with a first comparison with pneumatic actuators.

## II. WORKING PRINCIPLE AND DESIGN

The operation of the actuator relies on the forces exerted between a cylindrical magnet and a thick copper coil when current passes through the latter. Depending on the coil/magnet topology and current direction either repulsive or attractive forces can be created. In its simplest form, the actuator incorporates one permanent magnet and one coil within a silicone body. Figures 2a and 2b show the actuator in deactivated and activated form respectively. Bending of the actuator can be controlled precisely by adjusting the magnitude and direction of the coil current  $I$ .

Alternate configurations of magnets and coils can be selected in the design of an application employing this actuator; see Fig. 2c. For instance, when a single permanent magnet is used, configuration *B* results in better performance compared to configuration *A* in terms of bending angle at the expense of increased mass. In the case of multiple magnets, configurations *C* and *D* can be adopted. However, configuration *C* is not recommended for very powerful magnets since attractive forces between two consecutive magnets may be strong enough to reduce significantly or even to disallow bending. In such case, configuration *D* is more suitable, as it adds more space between two consecutive magnets and minimizes interference. Although no a priori size and complexity restrictions exist on a Mag-Net actuator, the rigid component masses must be considered in long or complex designs to ensure proper operation.

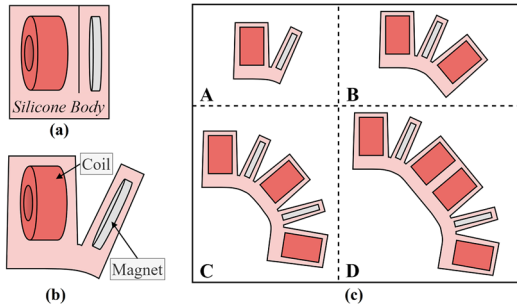


Fig. 2. Mag-Net actuator in its simplest form consisting of a single coil and a magnet. (a) Deactivated form,  $I = 0$ . (b) Activated form,  $I > 0$ . (c) Alternate configurations using one (A and B) or more (C and D) permanent magnets.

In developing the actuator, thick coils and cylindrical neodymium permanent magnets of the same geometrical and functional characteristics are used. Specifically, the coils of the prototype actuator built are made of 0.32 mm (28 AWG) copper winding wire, limiting the operating current to a

maximum value of 1.4 A [21]. Regarding the alternative coil winding technologies, the *wild*, *helical*, or *orthocyclic* options exist. For the prototype actuator, the orthocyclic winding technology is used, exhibiting an optimal filling factor of approximately 90%. Cylindrical neodymium magnets with high magnetization grade of N52 are selected. The silicone body is made of Elastosil M 4601 A/B silicone, with shore hardness 28A. To demonstrate this actuator technology, two applications are investigated: a soft two-fingered gripper and a crawling robot.

As shown in Fig. 3, the soft finger embodies two coils and a single magnet, according to configuration *B*. Both sides of the finger are extended; at the left (*rear part*) to allow coupling with the gripper's rigid body and at the right (*front part*) to increase its length and thus, the gripper workspace. The dimensions and other design parameters are given in Table I.

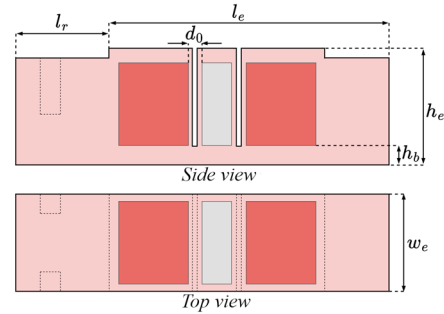


Fig. 3. Schematics of the prototype soft finger and main parameters.

TABLE I. PARAMETERS OF THE SOFT FINGER DESIGN.

Parameter	Value
Effective length ( $l_e$ )	41 mm
Effective height ( $h_e$ )	24 mm
Effective width ( $w_e$ )	22 mm
Rear part length ( $l_r$ )	20 mm
Coil-magnet initial distance ( $d_0$ )	0.9 mm
Bottom layer height ( $h_{bb}$ )	2.5 mm
Total finger mass	68 g

To demonstrate the effectiveness of the actuator in untethered soft robot applications, a crawling soft robot has been developed. This application allows for a qualitative assessment and, thus, only partial details are given here. The length of the robot's rear part was increased to withhold a lithium-ion polymer battery and a control board, while the bottom surface was extended with an extra silicone layer employing friction anisotropy to generate forward locomotion [22]. This was accomplished by creating a bottom surface structure of oblique teeth towards the rear part of the robot. The side view of the crawling robot design is shown in Fig. 4.

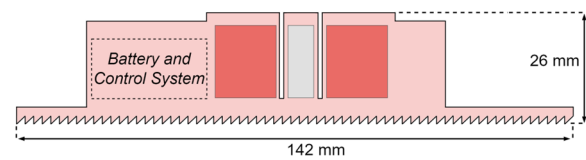


Fig. 4. Crawling soft robot utilizing friction anisotropy to move forwards.

## III. FINGER DYNAMICS MODEL

A simple yet accurate lumped-element model has been developed to describe the finger's motion along the vertical two-dimensional space. The Lagrangian approach has been

proposed in the past for modelling fPN actuators [23]; this is ideal for future development of real-time model-based control schemes. The finger is modeled as a 3-segment, 2-Degree-of-Freedom (DoF) planar open chain in gravity, with segment masses  $m_0$ ,  $m_1$  and  $m_2$ ; see Fig. 5. Due to design symmetry, each joint is subject to the same constant rotational stiffness  $k$  and damping  $b$  that can be determined experimentally. The driving forces  $\mathbf{f}_1$  and  $\mathbf{f}_2$ , i.e., the electromagnetic forces between a magnet and a coil, are applied at the center of the corresponding coil/ magnet. In the case of the magnet-embedded segment, this point coincides with the segment's center-of-mass (CoM). For the last segment, the CoM is shifted due to the mass of the finger's extended front part. Note that in the subsequent analysis, the electromagnetic forces exerted between coils are disregarded, since they form only a very small fraction of the forces exerted between coils and magnets; this assumption is validated in Section V through computational analysis.

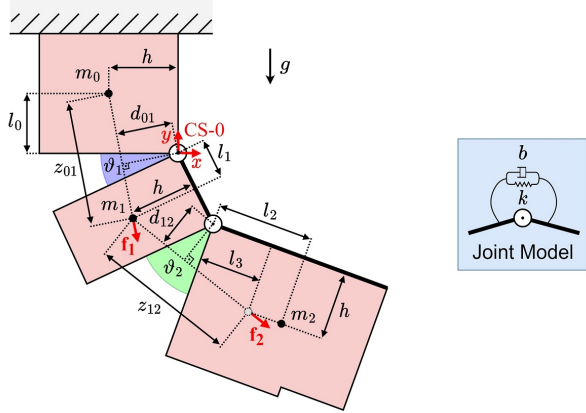


Fig. 5. The electromagnetic soft finger as a 2-DoF planar open chain and the joint model.

The coordinates  $[x_1 \ y_1]^T$  and  $[x_2 \ y_2]^T$  of the point masses  $m_1$  and  $m_2$  with respect to CS-0 can be calculated as follows

$$\begin{bmatrix} x_1 \\ y_1 \end{bmatrix} = \begin{bmatrix} l_1 \sin \theta_1 - h \cos \theta_1 \\ -l_1 \cos \theta_1 - h \sin \theta_1 \end{bmatrix} \quad (1)$$

$$\begin{bmatrix} x_2 \\ y_2 \end{bmatrix} = \begin{bmatrix} l_2 \sin(\theta_1 + \theta_2) - h \cos(\theta_1 + \theta_2) + 2l_1 \sin \theta_1 \\ -l_2 \cos(\theta_1 + \theta_2) - h \sin(\theta_1 + \theta_2) - 2l_1 \cos \theta_1 \end{bmatrix} \quad (2)$$

The kinetic energy  $E_K$ , the gravitational potential energy  $E_G$  (with respect to CS-0), and the elastic potential energy  $E_E$  of the soft finger are given by (3), (4) and (5) respectively.

$$E_K = \frac{1}{2} \sum_{i=1}^2 m_i (\dot{x}_i^2 + \dot{y}_i^2) \quad (3)$$

$$E_G = \sum_{i=1}^2 m_i g y_i \quad (4)$$

$$E_E = \frac{1}{2} \sum_{i=1}^2 k \theta_i^2 \quad (5)$$

Consequently, the Lagrangian function can be written as

$$L = E_K - E_G - E_E \quad (6)$$

The Euler-Lagrange equations are of the form

$$\tau_i = \frac{d}{dt} \frac{\partial L}{\partial \dot{\theta}_i} - \frac{\partial L}{\partial \theta_i} + \frac{\partial B}{\partial \dot{\theta}_i}, \quad i = 1, 2 \quad (7)$$

where  $\tau_i = (\tau_1, \tau_2)$  are the generalized forces, and  $B$  is the Rayleigh dissipation function given by

$$B = \frac{1}{2} \sum_{i=1}^2 b \dot{\theta}_i^2 \quad (8)$$

Substituting (1)-(6) and (8) in (7) results in the finger equations of motion in matrix form as

$$\boldsymbol{\tau} = \mathbf{M}(\boldsymbol{\theta}) \ddot{\boldsymbol{\theta}} + \mathbf{c}(\boldsymbol{\theta}, \dot{\boldsymbol{\theta}}) + \mathbf{g}(\boldsymbol{\theta}) \quad (9)$$

where  $\boldsymbol{\theta} = [\theta_1 \ \theta_2]^T$ , and the mass matrix  $\mathbf{M}(\boldsymbol{\theta})$ , vector  $\mathbf{c}(\boldsymbol{\theta}, \dot{\boldsymbol{\theta}})$  and vector  $\mathbf{g}(\boldsymbol{\theta})$  are given in (10)-(12).

To complete the analysis, the relations between the electromagnetic forces  $\mathbf{f}_1$  and  $\mathbf{f}_2$ , the coil current  $I$  and the generalized coordinates  $\theta_1$  and  $\theta_2$  are needed. The literature on the exerted forces between a permanent magnet and a thick coil focuses solely on analytical solutions for the axisymmetric problem [24][25]. Non-axisymmetric systems can be accurately studied using a finite element method, but this approach is not optimal for the development of real-time control schemes. As confirmed in Section V through experimental assessment, the application of an existing analytical solution [25] to this non-axisymmetric problem results in trivial prediction errors of the generalized forces  $(\tau_1, \tau_2)$  for a wide range of joint angles, and, therefore, present methods can be adopted with great confidence.

The axial force between axisymmetric cylindrical magnets and thick coils that consist of many turns both radially and axially can be calculated using a variety of analytical or integral methods [24]. Figure 6 shows a cross-section of the electromagnetic system along with relevant parameters.

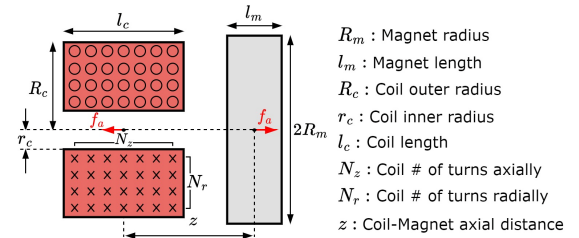


Fig. 6. Cross-section of an axisymmetric thick coil and cylindrical magnet system along with relevant parameters.

The method proposed by Robertson et al. represents each radial layer of turns as a separate thin coil [25]. The total

$$\mathbf{M}(\boldsymbol{\theta}) = \begin{bmatrix} m_1 (h^2 + l_1^2) + m_2 (h^2 + 4l_1^2 + l_2^2 + 4l_1 l_2 \cos \theta_2 + 4hl_1 \sin \theta_2) & m_2 (h^2 + l_2^2 + 2l_1 l_2 \cos \theta_2 + 2hl_1 \sin \theta_2) \\ m_2 (h^2 + l_2^2 + 2l_1 l_2 \cos \theta_2 + 2hl_1 \sin \theta_2) & m_2 (h^2 + l_2^2) \end{bmatrix} \quad (10)$$

$$\mathbf{c}(\boldsymbol{\theta}, \dot{\boldsymbol{\theta}}) = \begin{bmatrix} b \dot{\theta}_1 + 4l_1 m_2 (h \cos \theta_2 - l_2 \sin \theta_2) \dot{\theta}_1 \dot{\theta}_2 + 2l_1 m_2 (h \cos \theta_2 - l_2 \sin \theta_2) \dot{\theta}_2^2 \\ b \dot{\theta}_2 - 2l_1 m_2 (h \cos \theta_2 - l_2 \sin \theta_2) \dot{\theta}_1^2 \end{bmatrix} \quad (11)$$

$$\mathbf{g}(\boldsymbol{\theta}) = \begin{bmatrix} k \theta_1 + gm_1 (-h \cos \theta_1 + l_1 \sin \theta_1) + gm_2 (-h \cos(\theta_1 + \theta_2) + 2l_1 \sin \theta_1 + l_2 \sin(\theta_1 + \theta_2)) \\ k \theta_2 - ghm_2 \cos(\theta_1 + \theta_2) + gl_2 m_2 \sin(\theta_1 + \theta_2) \end{bmatrix} \quad (12)$$

exerted axial force  $f_a$  is calculated through superposition of the forces between each thin coil and the magnet as

$$f_a = \frac{1}{N_r} \sum_{n_r=1}^{N_r} F_s(R_m, r(n_r), l_m, l_c, z) \quad (13)$$

with

$$r(n_r) = r_c + \frac{n_r - 1}{N_r - 1} (R_c - r_c) \quad (14)$$

The term  $F_s(R_m, r(n_r), l_m, l_c, z)$ , given by (15), describes the force between a thin coil and the permanent magnet

$$F_s(R_m, r(n_r), l_m, l_c, z) = \frac{J_1 J_2}{2\mu_0} \sum_{e_1, e_2}^{(1, -1)^2} e_1 e_2 s_1 s_2 s_3 f_s \quad (15)$$

where  $J_1$  is the permanent magnet residual magnetization,  $J_2$  is given in (16), and  $f_s, s_1, s_2, s_3, s_4$  are intermediate algebraic expressions given by (17)-(19). Indexes  $\{e_1, e_2\}$  define the four terms of the summation resulting from the four pair combinations, i.e.,  $\{1, 1\}, \{1, -1\}, \{-1, 1\}$  and  $\{-1, -1\}$ .

$$J_2 = \mu_0 N_z I / l_c \quad (16)$$

$$f_s = K(s_4) - \frac{1}{s_2} E(s_4) + \left( \frac{s_1^2}{s_3^2} - 1 \right) \Pi \left( \frac{s_4}{1 - s_2} \middle| s_4 \right) \quad (17)$$

$$s_1 = z - (e_1 l_m + e_2 l_c) / 2, \quad s_2 = (R_m - r)^2 / s_1^2 + 1 \quad (18)$$

$$s_3 = \sqrt{(R_m + r)^2 + s_1^2}, \quad s_4 = 4R_m r / s_3^2 \quad (19)$$

In (17), functions  $K(s)$ ,  $E(s)$  and  $\Pi(s)$  are the complete first, second and third elliptic integrals respectively.

The generalized forces  $\tau_i = (\tau_1, \tau_2)$  can be written as

$$\tau_1 = f_1 d_{01}, \quad \tau_2 = f_2 d_{12} \quad (20)$$

where  $d_{01}$  and  $d_{12}$  are shown in Fig. 5 and calculated by (21). Based on (13), the magnitudes  $f_1$  and  $f_2$  of the electromagnetic forces can be estimated by substituting  $z$  with the corresponding coil-magnet axial distances as provided by (22). It is observed that the resulting forces are linearly proportional to the coil current  $I$ . The final equations of motion arise by substituting (20) to (9).

$$d_{01,12} = \frac{h(l_a + l_b) \cos \theta_a + (h^2 - l_a l_b) \sin \theta_a}{h(1 - \cos \theta_a) + l_b \sin \theta_a} \sqrt{1 + \frac{(l_a + l_b \cos \theta_a + h \sin \theta_a)^2}{(h(1 - \cos \theta_a) + l_b \sin \theta_a)^2}} \quad (21)$$

$$z_{01,12} = \sqrt{(h - h \cos \theta_a + l_b \sin \theta_a)^2 + (-l_a - l_b \cos \theta_a - h \sin \theta_a)^2} \quad (22)$$

where (21)-(22) yield  $d_{01}, z_{01}$  for  $l_a = l_0, l_b = l_1, \theta_a = \theta_1$ , and  $d_{12}, z_{12}$  for  $l_a = l_1, l_b = l_3, \theta_a = \theta_2$ .

## IV. FABRICATION

A multi-step, open casting process is followed to construct the soft finger. An overview of the individual steps is provided in Fig. 7. First, the Elastosil M 4601 silicone mixture is prepared and de-aired using a vacuum pump (step 1). Afterwards, it is poured into a 3D-printed Acrylonitrile Butadiene Styrene (ABS) mold to cast the main structure of the finger's silicone body (step 2). Next, the coils and the magnet are fully soaked into the remaining mixture for a few seconds (step 3). The prepared parts are allowed for 12h in room temperature to cure and then step 3 is repeated, but this time the coils are partially soaked leaving one side of the coil intact. This action is essential to minimize the distance between the magnet and the coils that depends on the thickness of the formed silicone membranes. In the next step, another silicone mixture is prepared to bond the main structure, the coils and the magnet (step 4). The finger is allowed to rest for at least 12h. Coil wires are extended using flexible silicone wires and connected to the control system described in Section V. Before operation, the silicone body is divided manually with caution in the denoted areas to permit free bending (step 5).

A nearly identical fabrication process is followed for the crawling soft robot. The procedure is extended by two more steps: the bottom surface structure with oblique teeth is bonded with the main silicone body and the electronic components are set in place. Finally, the rear part is filled with uncured silicone mixture and the robot is allowed to rest for 12h before being fully operational.

## V. RESULTS

### A. Soft Gripper

Comprehensive experiments have been conducted on the prototype soft finger to evaluate its performance. The finger is controlled by running either negative (Fig. 8b) or positive (Fig. 8c) current through its coils. Independent control of each DoF is feasible, e.g., by alternately driving the coils with positive and negative current as illustrated in Figures 8d and 8e. An overview of the finger control system is shown in Fig. 9a. A desktop computer produces high-level coil current control commands that are distributed through a serial interface to an Arduino Uno MicroController Unit (MCU) board. The current commands are interpreted by the MCU board and converted to Pulse Width Modulated (PWM) signals, which, in turn, are supplied to a DRV8871 H-bridge motor driver. Independent control of the finger's coils is not considered in the model and experiment comparison; thus, a single DRV8871 driver is sufficient to fully control the soft gripper while allowing for the generation of opposite direction currents. Coil current  $I$  is

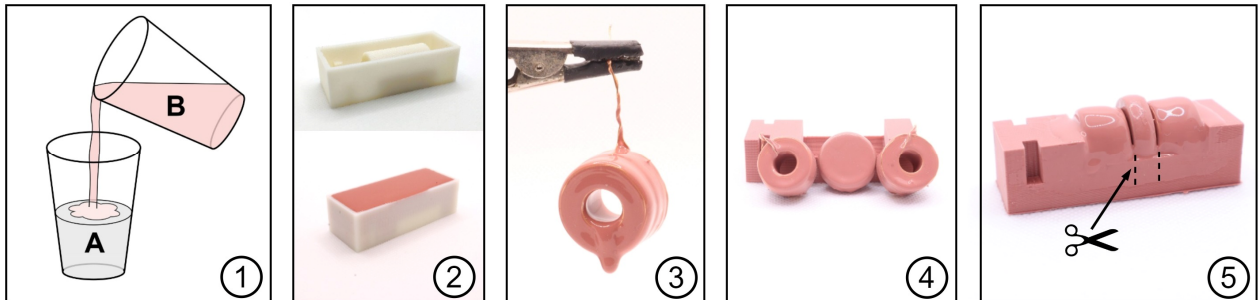


Fig. 7. Individual steps of the finger fabrication process. A similar process is employed for the crawling soft robot.

regulated by the duty cycle of the PWM input signal. When the duty cycle is set to 100%, current of 1.4 A is attained.

To determine the maximum grasping force that can be generated by the prototype finger, the experimental setup shown in Fig. 9b has been carried out. The finger is set to the vertical position against a 3D-printed obstacle. A calibrated force sensor made by Mitsui & Co. has been attached to the edge of the obstacle and aligned with the location of the fingertip. With a coil current of 1.4 A, the finger demonstrated maximum grasping force of 1.19 N. Higher forces can be generated if for a short period the current is increased over its nominal maximum value. When no current runs through the coils, a non-zero contact force (0.14 N), attributable to the finger's gravitational forces, is measured.

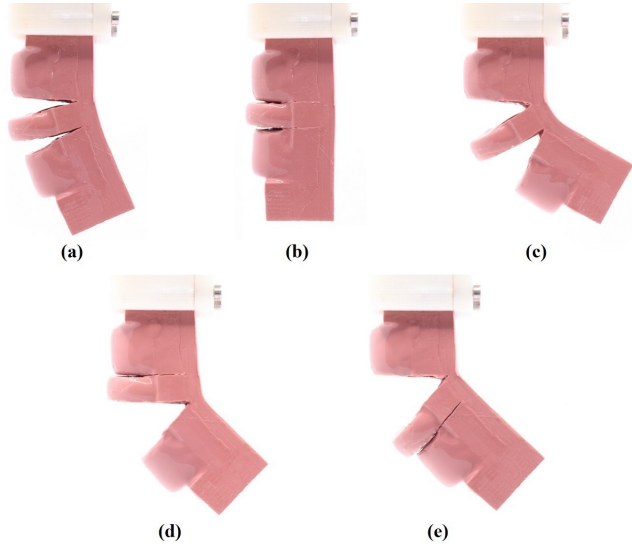


Fig. 8. (a) Prototype soft finger based on the developed actuator. The finger can be controlled by either (b) negative or (c) positive current running on both coils. Independent joint control is possible, also, as illustrated in (d) and (e).

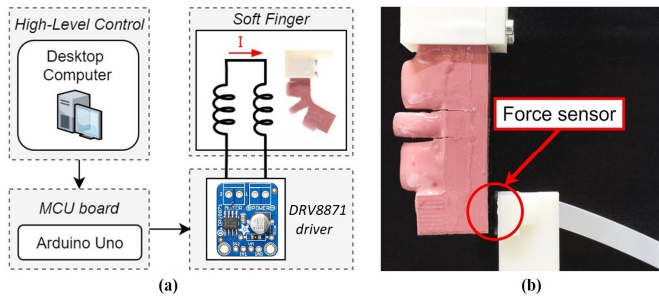


Fig. 9. (a) Soft finger control system overview. (b) Grasping force experiments. Maximum force of 1.19 N observed when current set to 1.4 A.

A camera-based system has been developed to record the finger's bending response, i.e.  $(\theta_1 + \theta_2)$ , against step and sinusoidal-input current commands. A Micro Quick Response (QR) code is attached to the fingertip using Sil-Poxy<sup>TM</sup> adhesive, while a high-speed camera (HiSpec 1, monochrome) is employed to record image frames at 2 kHz (Fig. 10a). To retrieve accurate estimations of the bending angle, the image frames are processed offline using a simplified algorithm that was originally developed for high-precision docking of mobile robots [27]. The algorithm is implemented in JAVA using an open-source QR-code recognition library [28].

For each experiment, the finger response is compared against predictions provided by the developed analytical model. The parameters of the model are given in Table II. The

stiffness coefficient  $k$  was determined experimentally by applying external force on the last segment with a handheld force gauge meter (RS Pro 5000G) and acquiring force samples for six distinct values of  $\theta_2$  (15°, 30°, 45°, 60°, 75°, 90°); see Fig. 10b. For each force measurement, the equivalent stiffness coefficient was determined, and their mean value was set as the joint stiffness coefficient  $k$ . The measurements are displayed in Fig. 11; very low variance of  $\sigma^2 = 0.26$  is observed. The damping coefficient  $b$  was identified by comparing data from eight dynamic experiments with model predictions, using the least-squares error minimization method.

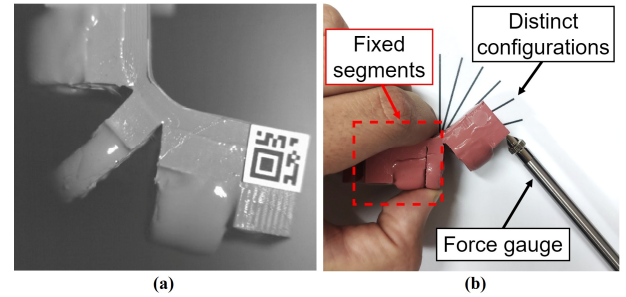


Fig. 10. (a) Image frame recorded by the high-speed camera. (b) Captured image during stiffness coefficient identification experiments.

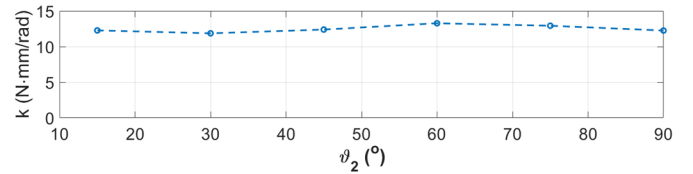


Fig. 11. Stiffness coefficient identification experiments.

TABLE II. PARAMETERS USED IN THE ANALYTICAL MODEL

Parameter	Value	Parameter	Value
$l_0 = l_3$	6.3 mm	$R_m$	10 mm
$l_1$	3.6 mm	$l_m$	6 mm
$l_2$	9.1 mm	$R_c$	9.5 mm
$h$	11.5 mm	$r_c$	3 mm
$m_1$	16.5 g	$l_c$	12 mm
$m_2$	22.5 g	$N_r$	15
$k$	12.5 N·mm/rad	$N_z$	30
$b$	0.129 mN·s/m	$J_1$	1.44 T
$g$	9.81 m/s <sup>2</sup>	$\mu_0$	1.256·10 <sup>-6</sup> N·A <sup>-2</sup>

The finger's response in four step input commands along with the corresponding model predictions and mean absolute errors are displayed in Fig. 12. Steady-state bending angle of 62.8° (Fig. 12) and maximum bending speed of 1491 °/s (Fig. 13) are realized when the current is set to 1.4 A. As shown in Fig. 12, the step-input responses suffer from ringing, indicating that the system is underdamped. It is possible to reduce ringing by increasing the height  $h_b$  of the bottom layer at the expense of reduced bending and grasping forces.

Comparisons of the sinusoidal-input responses and model predictions, and the corresponding mean absolute errors are shown in Fig. 14. The current command signals are given by

$$I_d = 0.7 \sin(2\pi ft) + 0.7 \text{ (A)}, \quad f = 0.5, 1, 2, 10 \text{ Hz} \quad (23)$$

A maximum peak-to-peak value is observed for the excitation frequency of  $f = 2$  Hz, while for  $f = 10$  Hz the

output's magnitude is significantly reduced. Mean absolute errors of  $0.98^\circ$  are observed for the step-input and  $1.09^\circ$  for the sinusoidal-input experiments.

Using two identical fingers, a soft gripper has been developed to assess soft finger performance in a variety of pick-and-place tasks. The gripper consists of a rigid 3D-printed body and the two soft fingers placed at an angle of  $30^\circ$  with respect to the gripper's longitudinal axis. Among other objects, the gripper successfully grasped and lifted a 93 g onion (Fig. 1), a 115 g lemon (Fig. 15a) and a 203 g wine glass (Fig. 15b). The latter task brought the gripper to its grasping limits ( $I=1.4\text{A}$ ) due to the target's high mass, low coefficient of friction and shape. Notably, only  $0.55\text{A}$  of coil current was required to firmly grasp and lift the 115 g lemon.

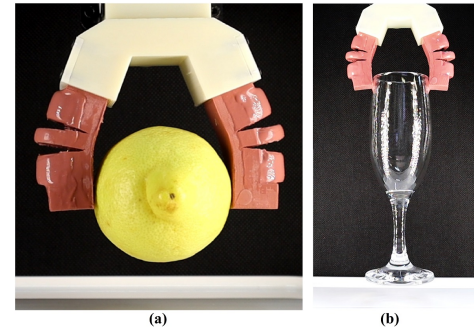


Fig. 15. Soft gripper lifts (a) a 115 g lemon and (b) a 203 g glass.

### B. Modelling Assumptions Validation

Regarding the first modelling assumption, i.e., that the interaction between coils can be safely neglected, a computational analysis has been conducted employing FEMM, an open-source tool for electromagnetic system simulation through the finite element method [26]. The axisymmetric ( $\theta_1, \theta_2 = 0$ ) representation of the finger's magnetostatic system is shown in Fig. 16a. When current of  $1.4\text{A}$  runs through *coil 1* and no current runs through *coil 2*, repulsive forces of  $f_a = 2.05\text{N}$  are exerted between coil 1 and the magnet. If the magnet is removed (Fig. 16b) and both coils are driven with maximum positive current of  $1.4\text{A}$ , the magnitude of the attractive forces between them is  $f_a = 0.024\text{N}$ , forming only a very small fraction (1.17%) of the forces exerted in the first case. Consideration of the coils mutual interaction would, therefore, increase substantially the computational complexity of the lumped-element model while leaving the accuracy of the bending predictions nearly intact. Hence, the forces exerted between coils are disregarded in the dynamics model.

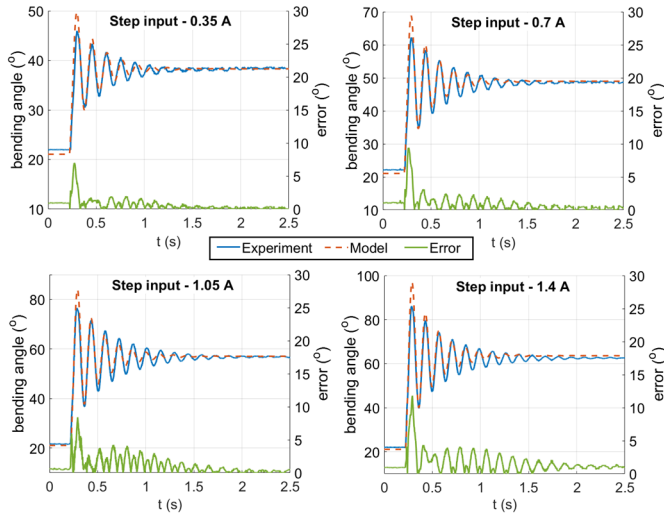


Fig. 12. Finger's bending response in step-input experiments.

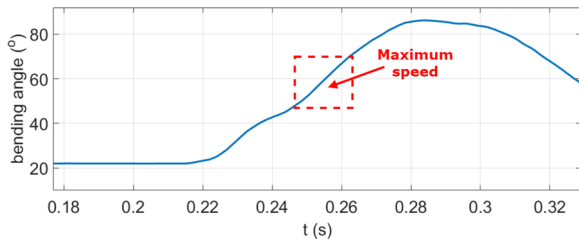


Fig. 13. Enlarged view of the finger's step-input response ( $I = 1.4\text{A}$ ). Maximum bending speed of  $1491^\circ/\text{s}$  is realized in the denoted area.

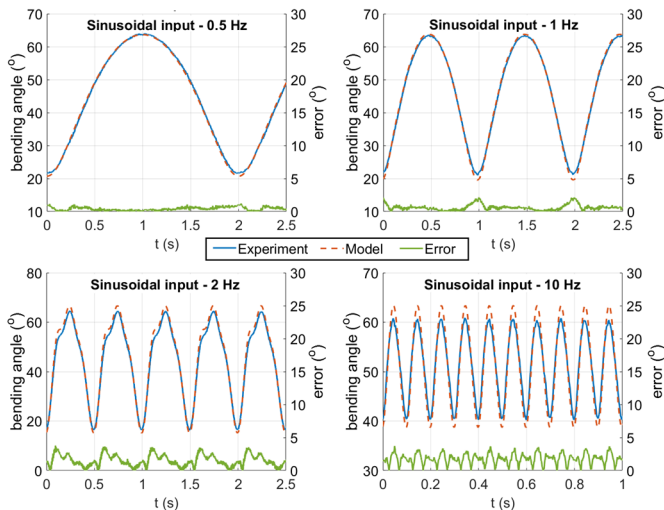


Fig. 14. Finger's bending response in sinusoidal-input experiments.

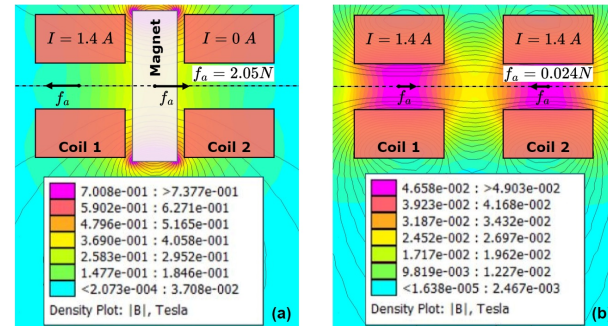


Fig. 16. (a) Flux density plot of the axisymmetric magnetostatic system representing finger's coil-magnet-coil configuration. When the magnet is removed (b), weak attractive forces of  $0.024\text{N}$  are exerted between coils.

For the second modelling assumption, the effects of applying the analytical solution described in [25] on a non-axisymmetric system are investigated. For this purpose, the experimental setup in Fig. 17a was carried out. The setup comprises a finger's joint rigid counterpart and a force gauge meter. The dimensions of the mechanism correspond to the values given in Tables I and II, with an exemption for parameter  $h$  which was increased by two millimeters ( $h = 13.5\text{mm}$ ) due to design constraints. The design adheres, also, to the initial ( $\theta = 0^\circ$ ) coil-magnet distance of  $d_0 = 0.9\text{mm}$ . With constant current of  $1.4\text{A}$  running through the coil, twelve measurements of the resulting torque with respect to the joint axis were collected, starting from  $\theta = 0^\circ$  and reaching up to  $\theta = 82.5^\circ$  in increments of  $7.5^\circ$ . To avoid magnet-probe interference, the measurements were acquired at a lateral distance of  $30\text{mm}$  from the joint axis. Figure 17b

compares experimental results with modelling predictions according to (20), (21) and (13). Mean absolute error of 0.21 N-mm was measured with the maximum error of 1.6 N-mm observed for  $\theta=15^\circ$ . The results, aligned with the model estimation errors shown in Figures 12 and 14, provide experimental validation of this modelling assumption.

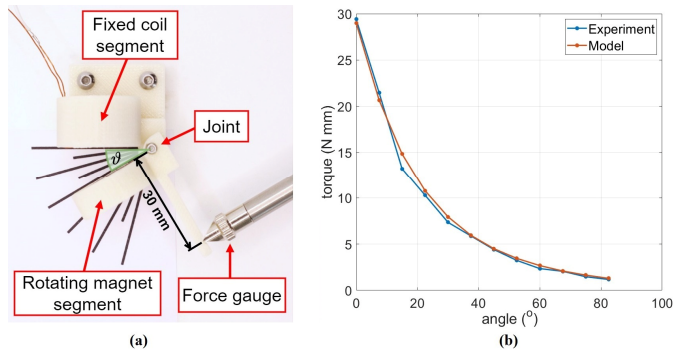


Fig. 17. (a) Rigid counterpart of a finger's joint. (b) Comparison between experimental results and model predictions.

### C. Crawling Robot

The soft crawling robot is shown in Fig. 18. To generate forward locomotion, a simplified control system has been developed with minimal space requirements. The system is powered by a single cell 150 mAh LiPO battery and utilizes a custom electronic board that produces current pulses at a predefined frequency of approximately 10 Hz. Figure 19 shows an overview of the system. A TLC555CP integrated circuit is preprogrammed with external resistors to generate a pulse series control signal that switches on and off a small-outline SS8050 NPN epitaxial silicon transistor. The coils are connected to the transistor's *drain* pin in parallel configuration to maximize the current that can be exerted by the single cell battery. When fully charged, the battery's terminal voltage is 4.2 V and the current  $I$  running through each coil is 1.05 A. For this experiment, the crawling robot has been positioned on a level area and turned on via a switch at its rear. Experimental results demonstrate that the robot was able to crawl forward by an average speed of 8.3 mm/s (Fig. 20).

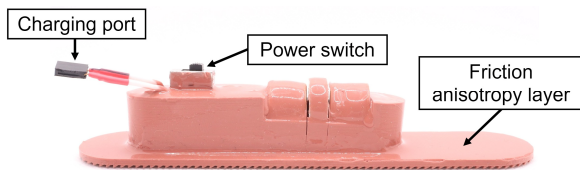


Fig. 18. The developed, entirely self-contained, soft crawling robot.

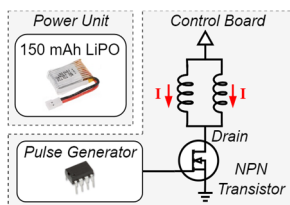


Fig. 19. Crawling robot control system overview.

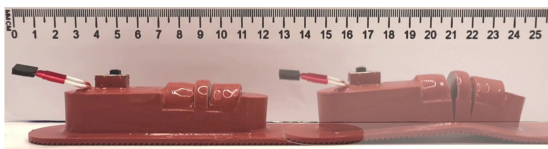


Fig. 20. Soft crawling robot moves forward by an average speed of 8.3 mm/s.

## VI. DISCUSSION

The presented electromagnetic actuator introduces both advantages and limitations compared to pneumatic counterparts. First, uninterrupted operation at maximum working current can damage the coils since the silicone body reduces heat dissipation noticeably. It was observed experimentally, though, that continuous operation of the developed soft finger in room temperature is feasible at approximately 80% of the theoretical maximum current, i.e.,  $\sim 1.1$  A. Also, Mag-Nets are characterized by higher power consumption and larger mass/ exerted force ratio when compared with pneumatic actuators, such as fPN; the developed crawling robot consumes 4.41 W and weights 91 g. However, if the mass of external driving subsystems involved in pneumatic actuation (compressors, electric valves etc.) is considered also, Mag-Nets have a clear lead. Furthermore, the duration of the fabrication process is relatively longer due to the increased number of silicone curing intervals. Approximately 36 hours are required in total to produce a soft electromagnetic finger, while a pneumatic equivalent would require 24 hours. Yet, the absence of highly strained thin walls, which, in the case of pneumatic actuators are sensitive to the presence of air bubbles in the silicone mixture, results in a trouble-free procedure overall. Additionally, operation of Mag-Nets actuators close to ferromagnetic materials should be avoided or attempted with caution to avoid harming the actuator or the target. Also, note that, the presented actuation design is confined to the production of bending motions. Other design approaches can be adopted to deliver the ability of elongation or twisting as in the case of specific pneumatic actuators. Yet, the effectiveness of these actuators is design/application-specific and, thus, it should be investigated individually.

On the other hand, the proposed actuator poses significant advantages. Control of a Mag-Net actuator is simpler and involves compact and lighter hardware compared to pneumatic counterparts that require bulky air compressors and electric valves to operate. This feature largely facilitates the development of untethered, entirely self-contained soft robots. Moreover, the dynamics of pneumatic systems and the inclusion of PID self-controlled pressure valves increase the response time and thus, add significant delays to the control loop. Instead, Mag-Net actuators respond virtually instantly upon a change on control current. Scalability is another advantage of the Mag-Nets. It is easy to produce sophisticated robots based on multiple, individually controlled actuating networks. Analogous pneumatic systems would involve complex designs with distinct pneumatic channels for each controllable DoF. Finally, Mag-Nets establish a cost-effective solution for the development of soft grippers. Table III summarizes the manufacturing and operating hardware expenses of the developed two-fingered soft gripper compared to a pneumatic equivalent. Notably, the total costs to produce the Mag-Net gripper represent only a small fraction (7.2%) of those of the pneumatic counterpart.

Regarding the developed lumped-element model, the experimental results validate its accuracy. Indeed, in the case of a 2 Hz sinusoidal input, the model predictions are fully aligned with the non-linear finger's response, indicating the model's ability to describe accurately the physics of the studied problem. Note though, that this modelling approach disregards the deformation of the silicone segments, and the presence of

high external forces could have a negative impact on the accuracy of the resulting predictions. Thus, depending on the characteristics of the design or application, caution must be exercised regarding the potential implications that may arise by adopting the rigid-segment modelling approach.

TABLE III. MAG-NET VS PNEUMATIC GRIPPER COSTS ANALYSIS.

<i>Fabrication</i>	<i>Mag-Net</i>	<i>Pneumatic</i>
Silicone body and 3D-printed molds	\$5	\$5
Other fabrication components	Coils (\$4), N52 Magnet (\$6), Power wires (\$1)	Pneumatic hoses (\$2)
Control System	DRV8871 board (\$8)	FESTO VEAB pressure regulator (\$450)
Electric Power/ Air pressure supply	Standard Power supply 24V 2A (\$20)	Standard Air compressor 4L (\$150)
<b>Total costs</b>	<b>\$44</b>	<b>\$607</b>

## VII. CONCLUSION

The application of existing electromagnetic actuators for soft robots is constrained due to several factors. This work introduced a novel current-controlled electromagnetic actuator that employs a cost-effective and compact design, produces substantial actuating forces, and thus, facilitates the development of untethered, entirely self-contained soft robots and grippers. The actuator incorporates coils and neodymium permanent magnets in a silicone body inspired by fPN actuators. Instead of LM coils, copper coils are employed, increasing substantially the exerted forces and extending the field of application of the presented actuator. During actuation, the bending resistance from the silicone body is minimal allowing high-speed bending motions and larger driving forces. Regardless of the use of rigid components, the actuator maintained the intrinsic compliance and flexibility of the entirely soft actuators. The design, dynamics modelling, and fabrication process of a prototype soft finger were presented thoroughly. Comprehensive tests on the prototype finger provided experimental validation of the developed analytical model and demonstrated maximum steady-state bending angle of 62.8°, maximum bending speed of 1491 °/s and 1.19 N of maximum grasping force at the fingertip. Based on the prototype finger, a soft gripper was developed and was effectively used in a variety of pick-and-place tasks. Finally, an entirely self-contained crawling robot was designed and manufactured that generated forward locomotion with an average speed of 8.3 mm/s, paving the way for a new design approach of autonomous soft robots.

## REFERENCES

[1] Seleem, I.A., El-Hussieny, H. & Ishii, H. "Recent Developments of Actuation Mechanisms for Continuum Robots: A Review," in *Int. J. Control Autom. Syst.*, vol. 21, pp. 1592–1609, 2023.

[2] El-Atab, N., Mishra, R.B., Al-Modaf, F., Joharji, L., Alsharif, A.A., Alamoudi, H., Diaz, M., Qaiser, N. and Hussain, M.M., "Soft Actuators for Soft Robotic Applications: A Review," in *Adv. Intell. Syst.*, vol. 2, 2020.

[3] M. S. Xavier *et al.*, "Soft Pneumatic Actuators: "A Review of Design, Fabrication, Modeling, Sensing, Control and Applications," in *IEEE Access*, vol. 10, 2022, pp. 59442-59485.

[4] Mosadegh, B., Polygerinos, P., Keplinger, et al., "Pneumatic Networks for Soft Robotics that Actuate Rapidly," in *Adv. Funct. Mater.*, vol. 24, 2014.

[5] Qing Xie et al., "Design and modeling of a hydraulic soft actuator with three degrees of freedom," in *2020 Smart Mater. Struct.*, vol 29, 2020.

[6] H. Shi, K. Tan, B. Zhang, and W. Liu, "Review on Research Progress of Hydraulic Powered Soft Actuators," in *Energies*, vol. 15, no. 23, p. 9048, Nov. 2022.

[7] F. Renda, M. Giorelli, M. Calisti, et al., "Dynamic Model of a Multibending Soft Robot Arm Driven by Cables," in *IEEE Transactions on Robotics*, vol. 30, no. 5, pp. 1109–1122, Oct. 2014.

[8] N. C. Chairopoulos, P. Vartholomeos and E. Papadopoulos, "Modeling, Simulation and Experimental Validation of a Tendon-driven Soft-arm Robot Configuration - A Continuum Mechanics Method," in *IEEE/RSJ International Conference on Intelligent Robots and Systems (IROS)*, Macau, China, pp. 5695-5700, 2019.

[9] Kheirikhah, M.M., Rabiee, S., Edalat, "A Review of Shape Memory Alloy Actuators in Robotics," in *RoboCup 2010: Robot Soccer World Cup XIV*, vol. 6556, 2010, pp. 206-217.

[10] D. J. S. Ruth, J.-W. Sohn, K. Dhanalakshmi, and S.-B. Choi, "Control Aspects of Shape Memory Alloys in Robotics Applications: A Review over the Last Decade," in *Sensors*, vol. 22, no. 13, p. 4860, Jun. 2022.

[11] Ebrahimi, N., et al., "Magnetic Actuation Methods in Bio/Soft Robotics," in *Adv. Funct. Mater.* 2021, vol. 31, 2005137, 2021.

[12] Kim, Y., & Zhao, X., "Magnetic Soft Materials and Robots," in *Chemical reviews*, vol. 122, pp. 5317–5364, 2022.

[13] W. R. Johnson, S. J. Woodman, and R. Kramer-Bottiglio, "An Electromagnetic Soft Robot that Carries its Own Magnet," *2022 IEEE 5th International Conference on Soft Robotics (RoboSoft)*, Edinburgh, United Kingdom, pp. 761-766, 2022.

[14] N. Hanqing, F. Ruoyu, X. Yuwei, et al., "MagWorm: A Biomimetic Magnet Embedded Worm-Like Soft Robot," in *Soft Robotics*, Oct 2021.

[15] Carpenter, J.A., Eberle, T.B., Schuerle, S., Rafsanjani, A. and Studart, A.R., "Facile Manufacturing Route for Magneto-Responsive Soft Actuators," in *Adv. Intell. Syst.*, vol. 3, 2000283, 2021.

[16] Mao, G., Schiller, D., Danning, D. et al., "Ultrafast small-scale soft electromagnetic robots," in *Nat. Commun.*, vol. 13, 2022.

[17] N. Kohls, B. Dias, Y. Mensah, B. P. Ruddy and Y. C. Mazumdar, "Compliant Electromagnetic Actuator Architecture for Soft Robotics," *IEEE International Conference on Robotics and Automation (ICRA)*, Paris, France, 2020, pp. 9042-9049.

[18] Guo, R., Sheng, L., Gong, H. et al., "Liquid metal spiral coil enabled soft electromagnetic actuator," *Sci. China Technol. Sci.*, vol. 61, 2018, pp. 516–521.

[19] Wang, Q., Lu, X., Yuan, N. and Ding, J., "Small-Scale Soft Robot with High Speed and Load Capacity Inspired by Kangaroo Hopping," *Adv. Intell. Syst.*, vol. 4, 2100129, 2022.

[20] Nemitz, M. P., Mihaylov, P., Barraclough, T. W., Ross, D., and Stokes, A. A." Using Voice Coils to Actuate Modular Soft Robots: Wormbot, an Example," *Soft Robotics*, vol. 3, pp. 198–204, 2016.

[21] M. E. Valkenburg, W. M. Middleton, "Reference Data for Engineers: Radio, Electronics, Computer and Communications", Ch. 49, p.16.

[22] N. Asawalertsak, F. Heims, et al., "Frictional Anisotropic Locomotion and Adaptive Neural Control for a Soft Crawling Robot", *Soft Robotics*, vol. 10, pp. 545–555, 2023.

[23] Z. Wang and S. Hirai, "Soft Gripper Dynamics Using a Line-Segment Model With an Optimization-Based Parameter Identification Method," in *IEEE Robotics and Automation Letters*, vol. 2, no. 2, pp. 624–631, April 2017.

[24] W. Robertson, B. Cazzolato, A. Zander, "Axial force between a thick coil and a cylindrical permanent magnet: optimising the geometry of an electromagnetic actuator," *The University of Adelaide. Journal contribution*, vol. 48, no. 9, pp. 2479-2487, 2019.

[25] W. Robertson, B. Cazzolato and A. Zander, "A Simplified Force Equation for Coaxial Cylindrical Magnets and Thin Coils," in *IEEE Transactions on Magnetics*, vol. 47, no. 8, pp. 2045-2049, Aug. 2011.

[26] K. Baltzis, "The FEMM Package: A Simple, Fast, and Accurate Open Source Electromagnetic Tool in Science and Engineering," *Journal of Engineering Science and Technology Review*, 2008.

[27] G. Bolanakis, K. Nanos and E. Papadopoulos, "A QR Code-based High-Precision Docking System for Mobile Robots Exhibiting Submillimeter Accuracy," *International Conference on Advanced Intelligent Mechatronics (AIM)*, Netherlands, pp. 830-835, 2021.

[28] Abeles, P., "BoofCV - An open-source library for real-time computer vision", 2016. [Online]. Available: <https://boofcv.org/>.